Transverse Photoresistivity from Photo-thermal Current Deflection in Metal Films

Cameron Grant

May 15, 2025

Contents

Department of Physics, Boston College, Chestnut Hill, MA, USA

Chapter 1

Nonlinear Photocurrent Measurement

1.1   Introduction

Most modern technology relies upon an ability to measure the intensity and character of incident light. Near-infrared waves carry billions in financial trades daily, radio waves tell of advancing aircraft, visible light and microwaves allow astronomers to catalog nearby asteroids and to determine the conditions of the early universe. In short, optical sensing—the conversion of light into measurable electronic signals—has become ubiquitous and essential. The potential to increase the specificity of that conversion, then, is of both economic and scientific interest. Nonlinear photocurrent presents precisely that potential. With a dependence on multiple components of the incident electric field, nonlinear responses are able to detect not only intensity, but also polarization [1, 2, 3, 4]. The resulting additional degrees of freedom have the ability to enrich data provided by modern optical sensors and, for example, multiplicatively increase the throughput of fiber-optic cables [5].

Before nonlinear photocurrent can be utilized reliably, however, there are significant experimental challenges to overcome. Foremost is the size of the response, which can be orders of magnitude smaller than zeroth- and first-order photocurrent effects. As a result, special care must be taken to isolate measurements from local electronic noise (see Section 2.2.2) and to minimize contribution from other opto-electronic sources (e.g. bolometric effects and photo-Seebeck) [6]. This thesis attempts to clarify and address the necessary experimental considerations for nonlinear photocurrent measurement. In addition, a novel bolometric response
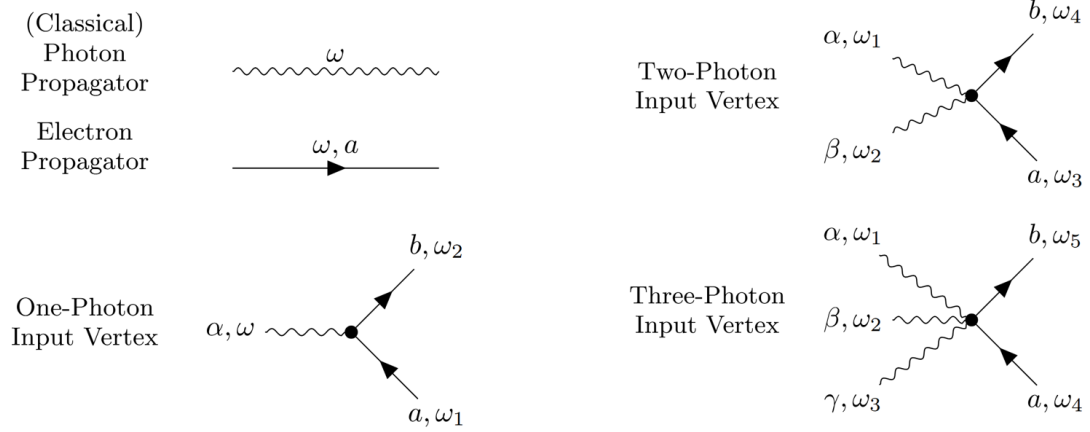
Figure 1.1: Feynman diagrams of photon input vertices for light-matter interactions, which comprise the higher-order terms in nonlinear photocurrent expansions. Electron and photon propagators are defined with frequency ω. Photons additionally carry spatial indices defined by Greek characters α, β, γ. Complete diagrams of higher-order interactions are not included here for simplicity, but are presented and discussed in detail by [7], from which these diagrams have been reproduced.

is highlighted which will, in principle, interfere with field-applied nonlinear photocurrent measurements in any thin-film device, regardless of material. Given its origin, we refer to this bolometric effect as "photo-thermal current deflection." A general methodology to minimize its impact in future research is presented.

1.2 Phenomenology

Microscopic physical processes can be expanded in terms of the number of interactions involved (see Feynman diagrams, Figure 1.1). Photocurrent generation is no exception, and is traditionally expanded phenomenologically as follows:

$$J_a = \sigma_{ab}^{(1)} E_b + \sigma_{abc}^{(2)} E_b E_c + \sigma_{abcd}^{(3)} E_b E_c E_d + ... \tag{1.1}$$

Where J_a is the current generated along direction a as a result of the applied electric field(s) E_i along direction(s) i, and $\sigma^{(n)}$ represents the n-th order conductivity tensor. The first order effect is well-studied; diagonal elements of $\sigma^{(1)}$ represent linear longitudinal conductivity, and off-diagonals describe linear Hall

2

conductivity. Importantly, first-order photocurrent responses depend on only one component of the incident electric field (E_b), and are therefore unable to differentiate between linear and circular polarizations. This motivates the study of second-order nonlinear photocurrent, which has no such limitations but presents other issues. Namely, in centrosymmetric systems (with $\sigma^{(2)}$ invariant under the inversion operator $\mathcal{I}$) second order photocurrent is forbidden by symmetry:

$$\mathcal{I}(J_a) = \mathcal{I}(\sigma^{(2)}_{abc}E_bE_c)$$
$$-J_a = \sigma^{(2)}_{abc}(-E_b)(-E_c)$$
$$-J_a = J_a$$

The large majority of natural materials, as well as many systems of interest in condensed matter research, are centrosymmetric, so this restriction is problematic. It can be circumvented, however, by breaking inversion symmetry artificially with a small external perturbation. To accomplish this, we apply a weak DC current, generating a static electric field and allowing measurement of (effectively) second-order photocurrent in materials with inversion symmetry by virtue of a third-order interaction:

$$J_a = (\sigma^{(3)}_{abcd}E_bE_c)E_d^{DC} \tag{1.2}$$

Where the second-order effect is enclosed in parentheses, and the applied perturbation E_d^{DC} allows the (now) *effectively* second-order photocurrent to be nonzero.

1.3 Experimental Considerations

1.3.1 Response Magnitude

The first challenge nonlinear photocurrent presents to the experimentalist is its magnitude. Nonlinear effects comprise multiple sequential light-matter interactions, each with some probability to occur. We can generally expect the occurrence of a nonlinear interaction, then, to be exponentially less likely than its constituent linear interactions. The result is a much smaller effect size, and a subsequent need for very high precision measurement. A solution to this problem, frequency locking, is discussed in detail within Section 2.2.
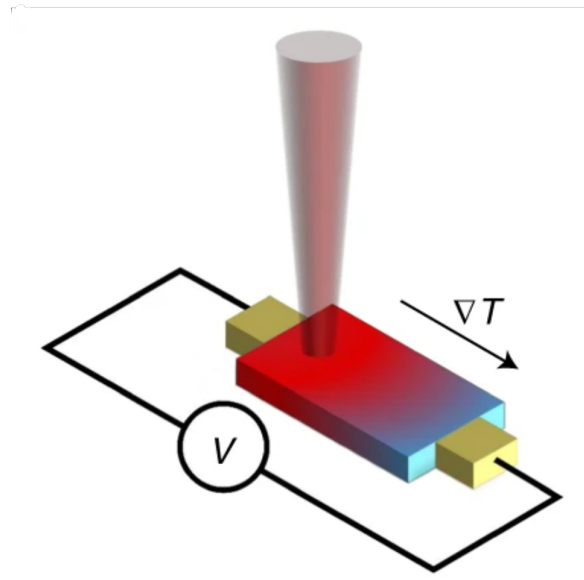
3

Figure 1.2: Image depicting the temperature gradient and photo-Seebeck response generated as a result of the incident beam. Reproduced, with permission, from [1]

.

1.3.2 Photo-Seebeck Effect

After contributions from environmental and electronic noise are removed, another difficulty becomes apparent. Generation of *nonlinear* photocurrent effects implies the presence of *linear* interactions as well. Without careful consideration, the magnitude of those linear interactions can saturate measurements or otherwise drown out nonlinear responses of interest.

One especially problematic interaction arises as a result of the Seebeck effect, discovered by the eponymous Thomas Johann Seebeck in 1822. The classical principle behind the phenomenon is simple. Heat, in a material, represents disordered particle motion. As a result, the presence of a thermal gradient ΔT will, statistically, result in a net flow of particles from areas of higher temperature to areas of lower temperature. In a crystal, positive charges are spatially constrained to a lattice structure so that thermal gradients cause a net flow of *only* the free charge carriers (electrons or holes) and, consequently, generate a voltage difference:

$$\Delta V = -S\Delta T \tag{1.3}$$

Where ΔV is the voltage generated and S is the Seebeck coefficient, which varies in magnitude and sign

4

between materials but is generally measured in $\mu V/K$ [8]. In addition to the charge carrier dispersion mechanism (described above), more recent research has also attributed some Seebeck effects to phonon drag, which are discussed in detail elsewhere (see [9]).

Seebeck effects arising from the first-order absorption of light in a material are, appropriately, called photo-Seebeck [2, 6, 10]. In measurements requiring a small spot size compared to the device under study, including many nonlinear photocurrent measurements, spatially localized heating from absorption results in a large photo-Seebeck voltage, and can pose a significant problem for precision measurements of other (more interesting) effects. To mitigate this issue, we (1) fabricate our both devices and contacts out of the same material (platinum or gold) to reduce material interface enhancement of Seebeck effects [11]; (2) design our devices to be highly symmetric to ensure even thermal loading; and (3) isolate the wire-bonded voltage leads far from the center of the device (using large electronic contacts) to allow any thermal gradients generated by the focused beam to equalize before voltage is measured.

1.3.3 Bolometric Effects

Bolometric effects encompass all phenomena that arise from a change in the conductivity of a material with respect to its temperature, or $\partial\sigma/\partial T$ [12]. The mechanism of that change, and explicit calculations of it for a given material, rely on band theory and other considerations. Nevertheless, the phenomenology is simple: An increased temperature causes higher energy bands to become populated—bands that will, in general, have different carrier masses and contribute differently to the material conductivity. In photocurrent measurement, some conversion of light into heat by the device or substrate is unavoidable, and so bolometric effects are ubiquitous. They can be mitigated by noting that photo-bolometry relies only upon first-order absorption and, thus, is independent of polarization. The subtraction of two measurements that differ only in the polarization of the incident light, then, will ensure any bolometric effects are eliminated. For an example of this technique, see [1].

Chapter 2

Experimental Design

In any photovoltage measurement setup, there are two main components: The optics, used to manipulate and direct light onto the sample, and the electronics, used to measure the resulting current (or voltage). These two aspects of our measurement are discussed below. Efforts to automate various aspects of measurement are also presented.

2.1 Optical Path and Alignment

The optical path serves two purposes: (1) To impart a specific polarization and frequency dependence on the laser beam; and (2) to direct and focus that laser beam onto the sample. In this experiment, we find the response has no polarization dependence and, for that reason, discussion of polarizers, quarter- and half-waveplates is omitted here. Frequency dependence is imparted upon the beam by an optical chopper rotating at 290Hz, which periodically blocks and unblocks the laser as it spins. The resulting frequency dependence of the laser (discussed in detail in Chapter 4) is utilized by the lock-in amplifier (see Section 2.2.2) to isolate the photovoltaic signal from environmental noise.

Once the beam has the desired properties, we use two 99% reflective silver mirrors on two-axis tilt mounts to direct it into a ZnSe lens, which focuses the approximately 1mm beam waist down to a spot size of $\sim 10\mu$m. Finally, a 50-50 beam splitter is positioned between the last mirror and the lens to collect reflected light from the sample and direct it into an MCT (mercury cadmium telluride) infrared detector.
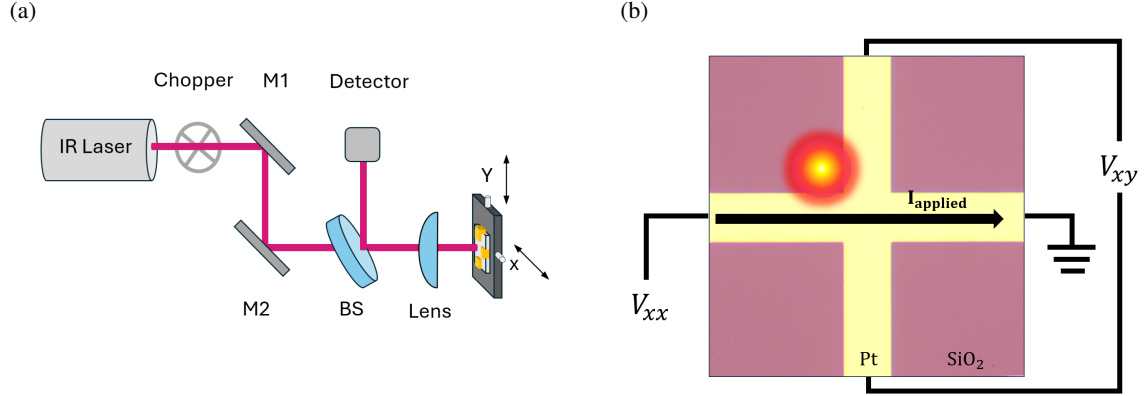
Figure 2.1: (a) A blueprint for our nonlinear photocurrent optical setup. Included are, in the order they are encountered by the laser beam, one optical chopper, two mirrors (M1 & M2), a beam splitter (BS), a plano-convex lens and the device, which is mounted on a set of linear translation stages. In addition, reflected light is redirected by the BS and collected by an IR detector for focusing and positioning purposes. (b) The electronic measurement setup annotated on a microscope image of the platinum cross device. Transverse (V_{xy}) and longitudinal (V_{xx}) voltage measurements are indicated, as well as the direction of applied DC current used to break inversion. The heating caused by the laser is illustrated in red. Device (Pt) and substrate (SiO$_2$) materials are labeled for convenience.

The detector is included, in part, to allow proper focusing of the beam onto the device. The quantity of light that reaches the detector will be maximized when the device is placed at the focal point of the lens; in any other position the reflected light will not perfectly be re-collimated, and will lose intensity as it travels back to the detector. Therefore, as the device is moved toward and away from the lens (called a 'focus scan'), the focal point will be indicated by the position of maximum detector response.

In addition to the position of the focal point, focus scans also provide invaluable information about the quality of the lens alignment. As one would expect, perfect lens alignment results in a single, sharply peaked gaussian curve. Improper alignment, either an off-center beam position on the lens or a non-orthogonal angle of incidence into the lens, will result in a much broader depth of focus, a weaker maximum intensity and, potentially, multiple peaks.

Finally, the detector allows precise positioning of the beam on the device. Specifically, the reflectance of the device and the substrate on which it rests are almost always noticeably different. Therefore, when the device is systematically moved in the plane perpendicular to the beampath (called a '2D scan'), the resulting intensity measurements provide an image of the device and the substrate (see Figure 2.4). This image is

subsequently used to place the beam spot at the desired position.

2.2 Electronics

The electronics used in the setup serve to isolate and to measure the voltage and current generated in the device by the laser. This responsibility is shared by two pieces of equipment, the pre-amplifier and the lock-in amplifier, described below.

2.2.1 Pre-Amplifier

True to its name, the pre-amplifier provides auxiliary filtering and gain before the signal is passed to the lock-in amplifier. Filtering is performed with a low- and a high-pass tunable filter, which together provide tunable band-pass frequency filtration. Typically the low-pass filter is set at three times the modulation frequency, and the high-pass filter at one-third the modulation frequency. If modulation is performed at 300Hz, this will eliminate all signals except those with frequencies between 30Hz and 3000Hz. The pre-amplifier can also add up to 50,000x gain, in cases when the signal strength is below the lock-in amplifier's optimal operating range. We use a Stanford SR560 pre-amplifier for the measurements presented in this thesis.

2.2.2 Lock-In Amplifier

The lock-in amplifier both isolates and measures electronic signals using a technique called frequency locking. Given an input signal and a reference signal of a single frequency (in our case, a sine wave at the frequency of chopper modulation), the lock-in amplifier extracts and measures the amplitude and phase of *only* the component of the input signal that oscillates at exactly the reference frequency. As a result, even with significant environmental noise and, for example, a large DC voltage background from an applied DC current, the lock-in amplifier is able to isolate a bolometric longitudinal signal of single μV magnitude (see Figure 2.4, far from the wire) generated by the laser. The 7230A lock-in amplifier used here allows tuning of the AC gain applied (0-90 db), the time-constant used for frequency integration ($5\mu s$ to 100ks), and the harmonic of the reference signal to use for frequency locking (1st to 127th).

Figure 2.2: One Stanford SR560 Pre-Amplifier, both front and back view. Visible on the front panel are the A and B voltage inputs, the filtered voltage output for both 50Ω and 500Ω impedances, various options for the applied gain, and settings for the high and low pass frequency filtration.

Figure 2.3: Ametek 7230A Lockin Amplilfier. The BNC connections are, from left to right, the A and B voltage inputs (used for differential voltage measurements), the reference signal input and the internal oscillating voltage output.

2.3   Automation

2.3.1 N-Dimensional Scans

As mentioned in Section 2.1, 1D (focus) and 2D scans using linear translation stages are essential to successful photocurrent measurement. In addition, measurements of effects with polarization dependence often call for scans in both quarter- and half-waveplate rotation angle, and measurements involving an external current require scans in the magnitude of current applied. Previous iterations of the photocurrent measurement setup used a separate, hard-coded program for each of these scan types. The resulting lack of standardization made data organization more difficult, and decreased flexibility. As a example, acquiring the polarization dependence of a response as a function of laser position required a full 2D scan to be taken and saved separately for *each* polarization angle of interest (typically five or more), and necessitated an operator manually inputting movement commands to the rotation stage before each 2D scan.

In order to resolve these issues, a program was developed capable of orchestrating N-dimensional scans using any combination of: X, Y and Z linear translation stages, two rotation stages, and a current source. For example, one could execute a four dimensional scan composed of size 20×20 2D scans in the x-y plane for each of four different current magnitudes and five polarization angles, resulting in a $20\times20\times4\times5$ output tensor. This output can then be viewed in arbitrary 2D slices from within the scanning program, and is saved using a standardized automatic naming convention. An example of a completed scan is provided in Figure 2.4.

2.3.2   Scan Queuing

In addition to a far more flexible scanning program, a master scan queuing system was created that allows multiple scans of different types to be queued and to run in sequence, with no intermediate human input. The result is the ability, for example, to queue a focus scan, a 2D reflectance scan, and five other 2D photovoltage scans with different current, polarization, and measurement settings; and have all seven scans completed and automatically saved overnight. For added convenience, the outcomes of all previous scans are available for the user to peruse inside of the scan queue program, and whole sequences of scans (both completed and queued) can be saved and reloaded at the click of a button. An image of the scan queue program's GUI is provided below (see Figure 2.5).
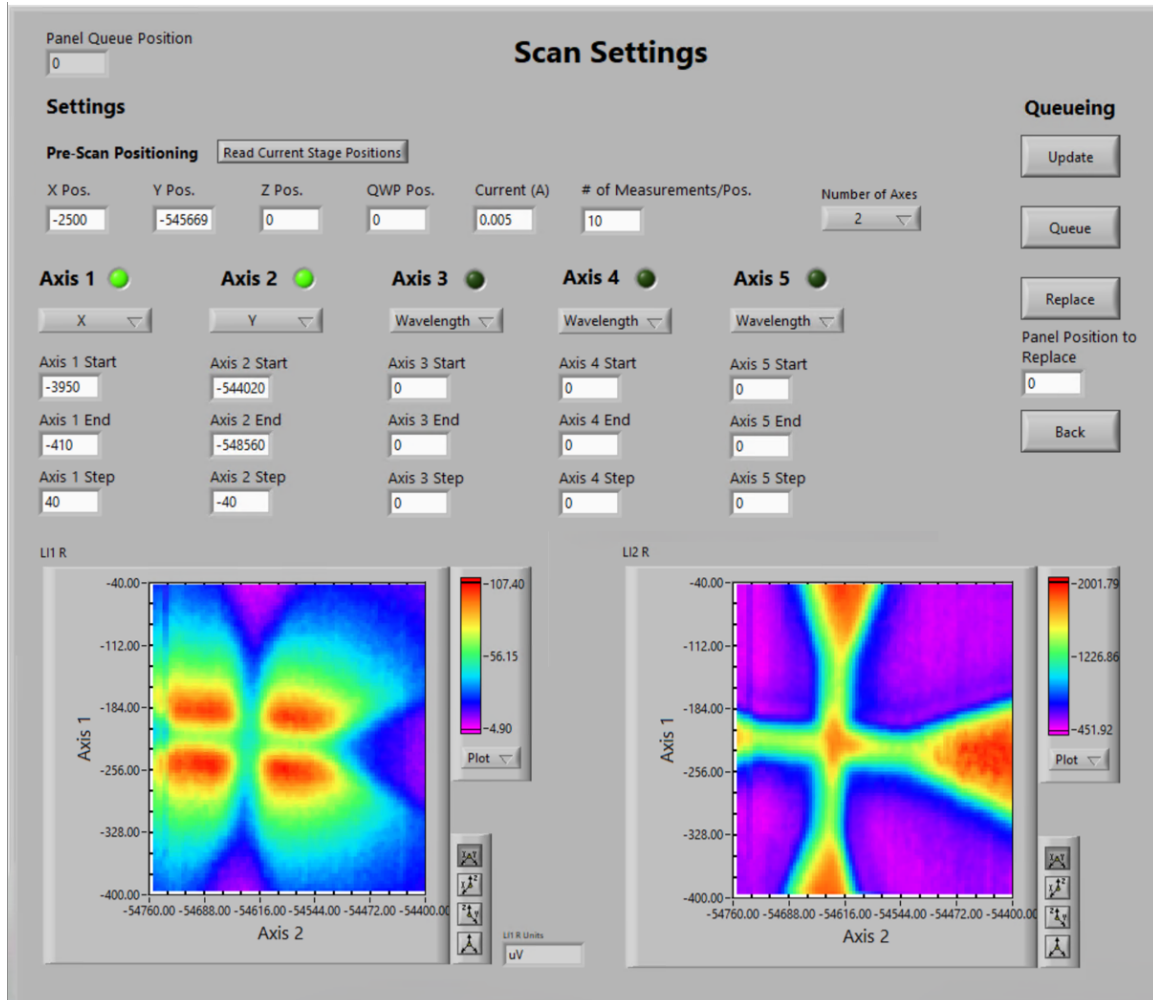
Figure 2.4: The results page of a completed scan. Preliminary settings (including the Z position of the focal point and DC current applied) are indicated beneath the 'Pre-Scan Positioning' section. Users can choose the number of axes (dimensions) to scan over, and then select the type of each axis from among: DC current applied, X, Y, Z, QWP Angle, HWP Angle, or wavelength. Completed scans display the output of the scan beneath their settings; this particular scan measured longitudinal photovoltage as a function of the laser's X-Y position on the device, with 5mA of current applied horizontally across the device (plotted in the bottom left). The magnitude of reflected light was measured concurrently by the MCT detector, the results of which, plotted in the bottom right, indicate the position and shape of the (platinum cross) device.

Figure 2.5: User interface for scan queuing software, with fourteen scans completed and one yet to be run (indicated by the green lights beside each queued scan). Scans can be queued either by adding a completely new scan (top left), or by duplicating and editing the settings of a previously queued scan, accessible using the 'Edit/Results' button. Quarter-waveplate and linear translation stage positions can be manually adjusted using an integrated 'Stage Control' option, which opens a custom control panel GUI. The scan queue program can be set to run sequentially without human input, or to pause between scans to allow for changes to later scans informed by preliminary results.

Chapter 3

Photo-thermal Current Deflection

3.1 Motivation

Given the novelty of field-applied second-order nonlinear photocurrent measurement, and the concerns detailed in Section 1.3, we chose to perform a control experiment in simple metal thin films to verify our experimental setup before exploring more interesting materials. For this purpose we fabricated symmetric crosses out of gold and platinum (see Section 3.3.1), expecting to measure a standard bolometric effect in longitudinal photovoltage, and no transverse response. Instead, when performing measurements of the latter, we discovered a novel *transverse* bolometric effect we call "photo-thermal current deflection." The experimental and simulated measurements of longitudinal and transverse photovoltage are presented below, as well as a phenomenological explanation for each. In addition, the dependence of the transverse response on laser power, applied current magnitude, frequency, device linewidth, and device material are presented, and shown to be in agreement with the proposed phenomenology.

3.2 Results

3.2.1 Longitudinal Photovoltage

Both the magnitude and character of the measured longitudinal photovoltage were expected. As explained in Section 1.3.3, metals have temperature dependent resistivity. When absorbed light causes the metal device to
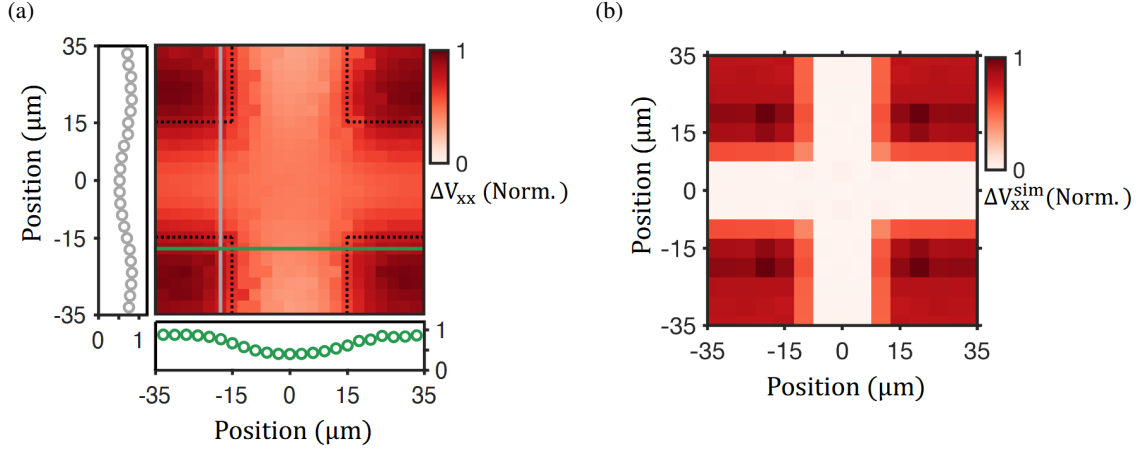
Figure 3.1: (a) Longitudinal voltage V_{xx} measured as a function of laser position on the device. Device edges are delineated by dashed black lines. Two linecuts are provided to illustrate voltage dependence on laser position parallel and perpendicular to the applied current direction (horizontal). (b) COMSOL simulation results performed using an identical current magnitude, linewidth, device material, and substrate material. The laser is modeled as a gaussian heat source.

heat up, then, we expect the longitudinal voltage generated by our applied DC current to change accordingly (by Ohm's law, $V = IR$). The seeming mystery of Figure 3.1(a) is that the longitudinal response is *smallest* when the laser strikes the metal device directly, and largest when the laser is positioned on the adjacent substrate. There is, however, a simple explanation: Platinum and gold, out of which the devices are made, are nearly perfect reflectors of MIR light [13]. The substrate, on the other hand, has non-negligible absorption in the MIR range, enhanced by its layered Si/SiO$_2$ structure [14]. As a result, significantly more heat is generated when the laser hits the substrate, which consequently raises the temperature of the neighboring metal device and causes the observed longitudinal bolometric photovoltage. In light of this explanation, the dependence of the longitudinal response is completely reasonable. The bolometric effect is maximal when the laser is positioned just beside the metal, decreases as it moves further away from the horizontal current-carrying wire (the gray linecut), and remains constant as it moves alongside the current-carrying wire (the green linecut).
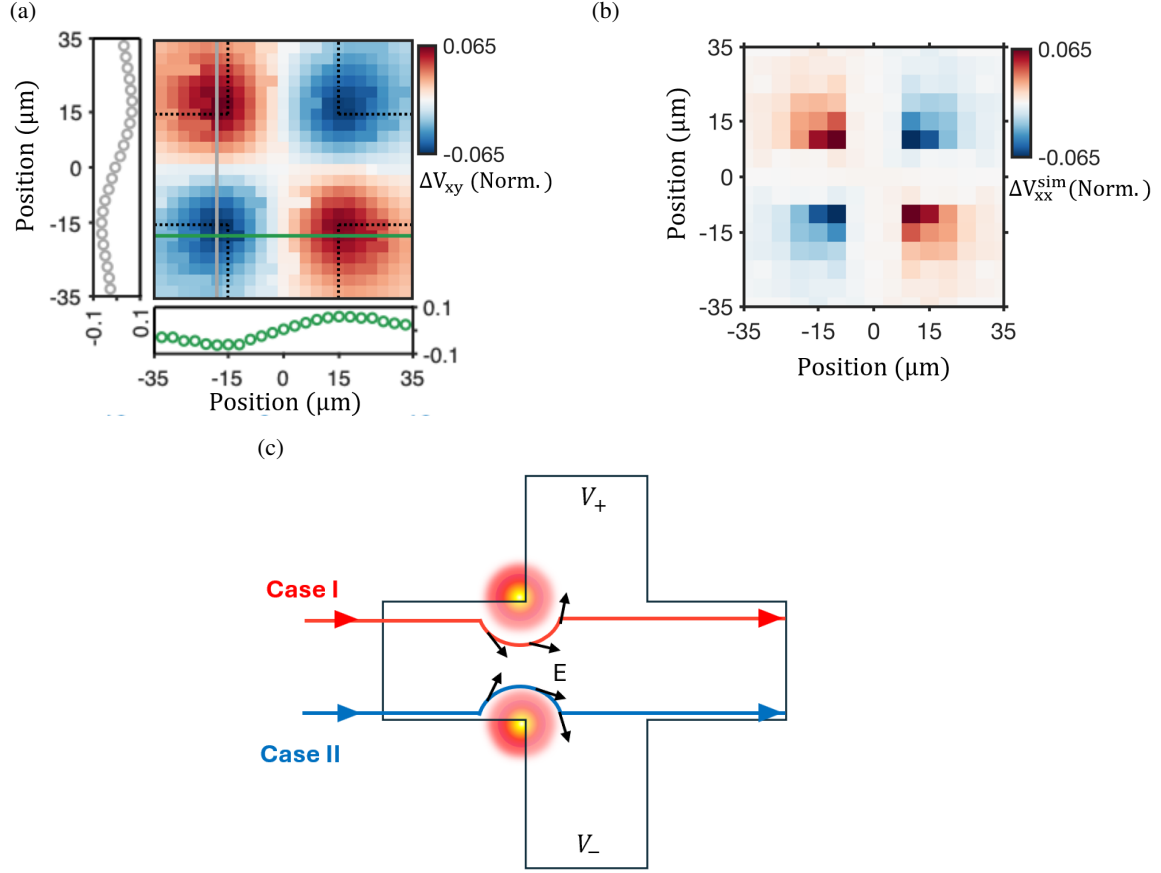
Figure 3.2: (a) Transverse photovoltage V_{xy} measured as a function of laser position on the device. Device edges are once again delineated by dashed black lines. Linecuts are provided to illustrate the asymmetric quality of the response in both parallel and perpendicular directions to the horizontal current applied. (b) COMSOL simulation results acquired using an identical current magnitude, linewidth, device material, and substrate material. The laser is, as before, modeled as a gaussian heat source. (c) Phenomenological illustration of the 'photo-thermal deflection' effect. In Case I, an area of local heating caused by the laser in the top left corner of the cross causes the applied DC current to deflect downward, then rebound towards the positive voltage lead. In Case II, the laser is moved to the bottom left-hand corner of the device, and the corresponding direction of deflection is reversed.

3.2.2 Transverse Photovoltage

Neither the magnitude nor the character of the measured transverse photovoltage were expected. In principle, since gold and platinum have largely uninteresting quantum geometry at room temperature, nonlinear transverse photovoltage effects should be negligible. In addition, there have been no reports of material-independent

linear effects present in platinum and gold capable of generating a transverse response. Nevertheless, we measure a finite transverse photovoltage that is independent of device material (gold or platinum), substrate material (sapphire or silicon), device linewidth (2μm, 10μm, or 30μm), and incident light polarization.

We attribute this effect to a zeroth-order novel bolometric mechanism we call "photo-thermal current deflection." The principle of the effect is as follows: When the laser is positioned just beside the corner of the metal cross, absorption by the substrate generates heat, which locally increases the resistivity of the metal in that corner. As a result, the applied DC current avoids, or is 'deflected' around, that corner of the device in favor of areas with lower resistivity. As illustrated in Figure 3.2(c), this 'current deflection' causes a net movement of electrons in the transverse direction, and is measured as a transverse photovoltage.

Since this effect can obscure measurement of genuine nonlinear responses, it is worth discussing briefly how best to remove it from future measurements. We propose two modifications to current experimental procedures. First, in those experiments for which laser intensity is not an issue, ensuring the spot size is larger than the device would ensure little to no current deflection given the even symmetry of the effect. On the other hand, if a tightly focused spot is necessary, ensuring that the device is perfectly symmetric and the beam is well-centered will mitigate the effect, again by virtue of its symmetry.

In the following sections, we present the dependence of the measured transverse photovoltage on various tunable factors, and confirm the effect is linear in nature. Furthermore, given the qualitatively and quantitatively successful simulations performed with COMSOL [15], in which the laser is modeled as *only* a local heat source, we argue that the "photo-thermal deflection" mechanism described above is the most simple and fitting phenomenological explanation for the measured effect.

3.2.3   Linewidth and Material Dependence

We first examine the impact of device linewidth and material on the magnitude of the measured transverse photovoltage. Phenomenologically, we expect the magnitude of the effect to decrease significantly with decreasing device linewidth; as the size of the current-carrying wire decreases, the net thermal gradient across the wire necessarily decreases, as well. As illustrated in Figure 3.3(a), both the simulated and experimental data reflect this dependence.

In addition, since neither platinum nor gold exhibit electronic or phononic excitations in the MIR, we would expect the magnitude of the effect to remain the same across both materials. We observe, however, an
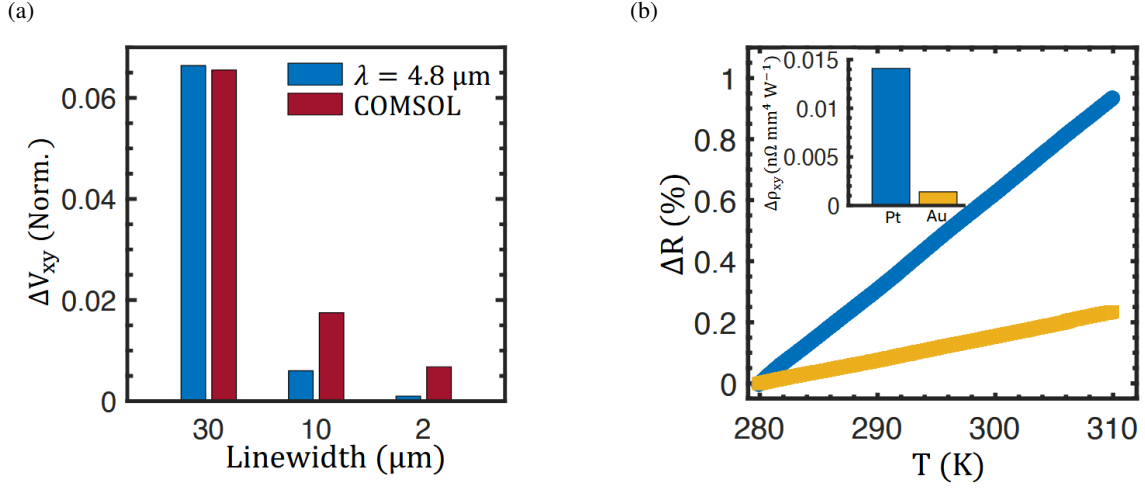
16

(a)   (b)

Figure 3.3: (a) Maximum transverse voltage response V_{xy} plotted as a function of device linewidth, both for experimental and simulated measurements. (b) Percentage increase in platinum and gold resistivity as a function of temperature above 280K. Inset is a plot of the transverse photoresistivity calculated using results from Figure 3.2(a). The larger temperature dependence of platinum's resistivity is reflected in a larger transverse photoresistivity, suggesting a bolometric origin for the effect.

order of magnitude larger response in platinum than in gold. This lends heed to a bolometric origin, given the dependence of resistivity on temperature is significantly higher in platinum than gold; see Figure 3.3(b). As a result, the applied current is deflected more strongly in platinum, and the measured transverse photovoltage is larger.

3.2.4 Power, Current, and Frequency Dependence

We now turn to the power and current dependence of the result. For nonlinear effects, the dependence of the response on both laser power and applied current should be nonlinear (see equation 1.2). Nevertheless, we measure a linear dependence on both variables (Figure 3.4), suggesting that the response is due to a zeroth-order effect, of which bolometric effects are one type. In addition, nonlinear effects should exist at higher harmonics of the fundamental laser modulation frequency. The measured response, however, exists largely at the first harmonic ω, again in line with predictions from the phenomenological explanation presented in Section 3.2.2. While the components of the transverse response measured along the second and third harmonics of the fundamental frequency are finite, they can be attributed to experimental artifacts from the nature of the chopper modulation. For more details, see Chapter 4.
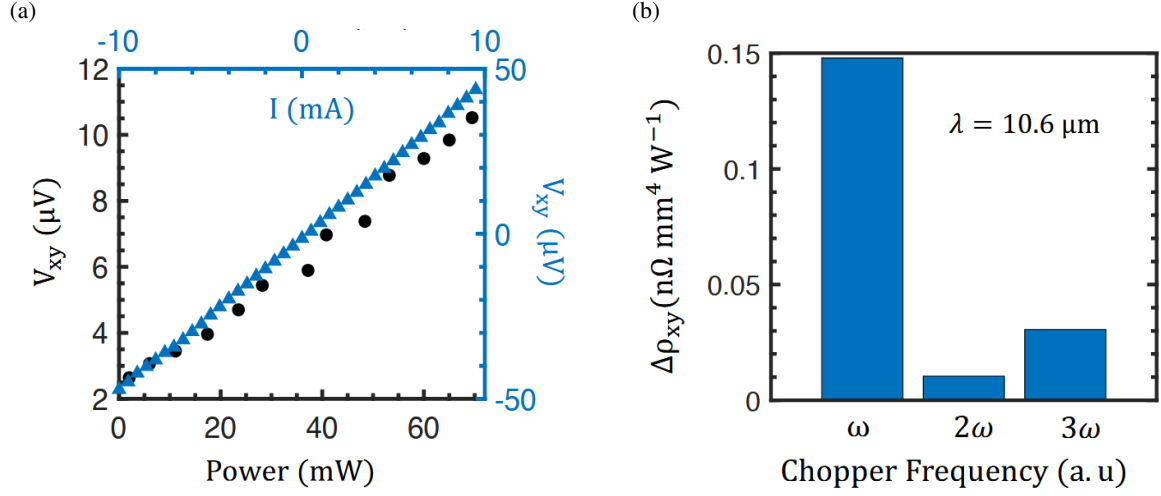
17

Figure 3.4: (a) Power (bottom axis) and current (top axis) dependence of the transverse photovoltage measured in platinum. Linear dependence in both suggests this transverse effect does not have a non-linear origin. (b) Frequency dependence of the transverse response, plotted in multiples of the modulating chopper frequency.

3.3   Equipment and Experimental Methods[1]

3.3.1   Device Fabrication

Our devices comprise 45 nm thin metal films (Pt, Au) deposited via e-beam on a 285 nm SiO_2/Si substrate (p doped). The device was patterned using a bilayer photoresist (LOR1A/S1805) and a laser mask writer (Heidelberg Instruments). The lift-off process was performed using Remover PG (MicroChem). All fabrication was performed in a cleanroom-in-a-glovebox to minimize contamination [17].

3.3.2   Photovoltage Measurement

Two tunable MIRCAT Mid-IR Lasers were used in Continuous Wave mode, with wavelengths in the ranges of 4.5 - 5.4 μm and 10.1 - 11.1 μm. The laser was modulated using a SciTec Instruments (Model 300CD) mechanical chopper at 197 Hz. This AC modulation of the electronic response was measured with an SRS830 Stanford or Ametek (Model 7230A) lock-in amplifier. The modulated laser beam is passed through a beamsplitter to redirect the light reflected by the sample onto an infrared detector (either from Hamamatsu

---

[1]Reproduced from [16]

18

Photonics or Amplied MCT detector from Daylight, depending on wavelength), allowing for the simultaneous collection of optoelectronic and reflectance data. A plano-convex ZnSe lens was used to focus onto the sample with spot size $\sim$11.7 μm for 4.8μm ($\sim$50.4 μm for 10.6μm) determined by standard knife-edge measurements.

3.3.3   Transport Measurement

The temperature-dependent transport measurements were taken using a two-point probe technique. The DC current was applied using a Keithley 6221 Precision Current Source, and the resulting voltage was measured with a Multimeter (Keysight 34461(a)).

3.3.4   Simulation

The longitudinal and transverse photovoltage response was simulated using the COMSOL Multiphysics 6.1 [15] with the electric currents, circuits, and heat transfer in solids modules. The geometry for the simulation was 200 μm $\times$ 200 μm $\times$ 800 μm slab of silicon underneath a 300 nm thick layer of silica glass. On top of the silica, platinum films were aligned along the x and y directions with dimensions: 45 nm thick, 30 μm wide, and 200 μm long. The current was applied along the x direction. A circular Gaussian heat source of spot size 17 μm was used to simulate the laser heating. The power absorbed by the silica substrate was assumed to be arbitrarily small (5 mW), and the power reflected by the platinum set at 99% that of the silica [13]. The position of the heat source was scanned from -35 μm to 35 μm in both the x and y direction in 5 μm increments centered on the platinum film to create a grid of 'photovoltage' measurements.

Chapter 4

Spectrum of Chopper Modulation[1]

4.1   Introduction and Definitions

Here we consider the frequency spectrum imparted on the laser beam as a result of modulation by an optical chopper. To first approximation, we assume a line-like beam (with no spatial extent) and a two-dimensional chopper. The resulting intensity waveform is a square wave, and includes all odd harmonics of the fundamental chopper frequency ω. Unfortunately, this simple analysis fails to explain the frequency dependence observed in the transverse photocurrent response, both in terms of the magnitude of the 3ω response and the existence of a 2ω response. Below, we address these two issues by considering both a gaussian beam profile and a finite chopper width.

   We approach the problem using three sets of coordinates, with the center of the chopper as the origin of each (see figure 1). These are: Cartesian coordinates normal to the beam path (x, y); cartesian coordinates in-plane with the chopper $(x', y) = (x/\cos(\eta), y)$; and circular coordinates in-plane with the chopper $(r, \theta) = (x'^2 + y^2, \mathrm{atan2}(y, x'))$. Here η is the angle between the plane normal to the beam path and the plane of the chopper, and atan2 is the two-argument arctangent function. Subsequent equations are presented using the most intuitive coordinate system, and transformations between coordinate systems are implied.

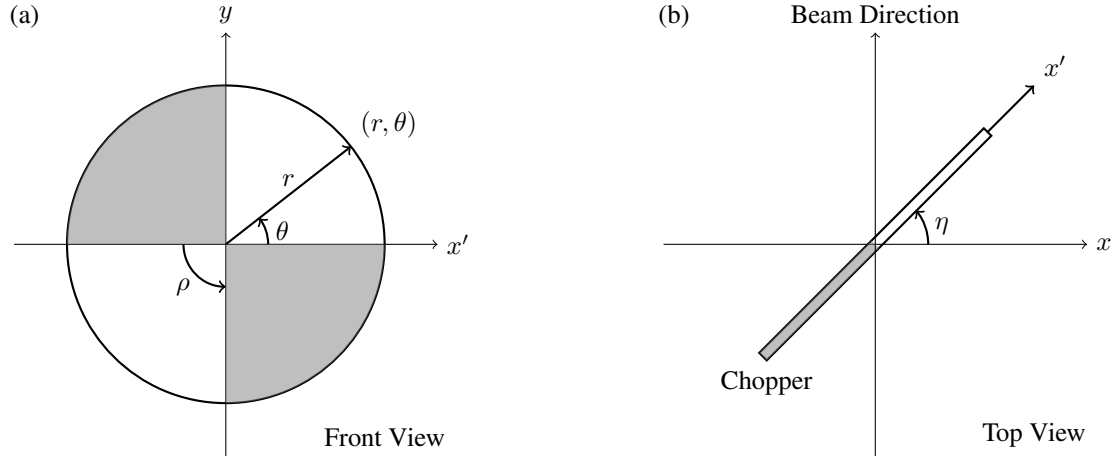[1]Reproduced from [16], supplementary information.

Figure 4.1: (a) Front view of the chopper blade with coordinates (x', y) and (r, θ), as well as cutout angle ρ, labeled. Shaded regions represent the blocked parts of the chopper. (b) Top down view of the chopper blade and the direction of the beam path. The chopper axis x' and the angle η between axes x and x' are labeled. The y axis is out of the plane.

4.2 Analysis

At a finite angle η, the front and back surfaces of the chopper are offset in the (x, y) plane (see figure 2), and therefore intersect the beam path at different times. For simplicity, we assume from here onward that the beam passes through the chopper plane in the first quadrant, that η is constrained by $0 < \eta < \pi/2$, and that the chopper rotates clockwise, as in figure 2. The beam is initially unblocked. As the chopper rotates, the leading edge of the front surface (highlighted in blue) intersects the beam first, and immediately blocks it. The leading edge of the back surface intersects the beam next, but is "hidden" behind the front surface, and has no effect. The trailing edge of the front surface similarly has no effect. Finally, as the trailing edge of the back surface (highlighted in red) intersects the beam path, the beam is unblocked. Compared to a 2D chopper, for which the front surface both blocks and unblocks the beam, the 3D chopper, with the same period of oscillation, blocks the beam for longer. With a finite angle η and chopper width w, then, the intensity modulation of the beam must exhibit an uneven duty cycle (DC). Given a point in (r, θ) coordinates, the corresponding duty cycle can be calculated as:

$$\text{DC} = 50(1 - |\frac{\delta\theta}{\rho}|) \tag{4.1}$$

Where ρ is the angle subtended by one chopper cutout (see figure 1), and $\delta\theta$ is the angle between the trailing

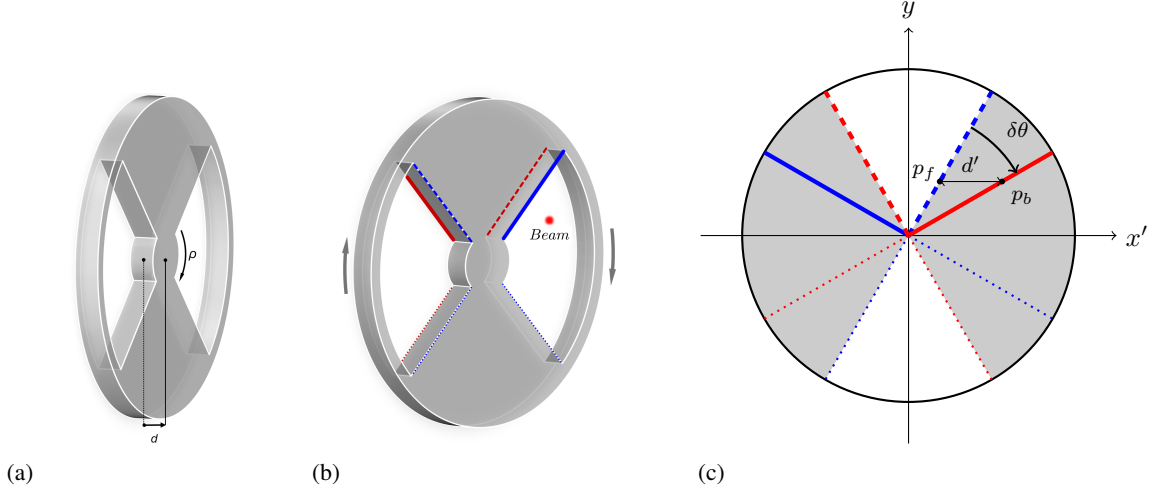(a)   (b)   (c)

Figure 4.2: (a) A 3D model of the chopper blade in (x, y) coordinates, with the cutout angle ρ and offset d labeled. (b) A 3D model of the chopper blade showing the front and back surfaces, the clockwise rotation direction, and the beam intersection point. Highlighted on the top half of the chopper are the leading edge of the front surface (blue), the leading edge of the back surface (red, dashed), the trailing edge of the front surface (blue, dashed) and the trailing edge of the back surface (red). (c) The same system as in (b) rotated 90 degrees, with the beam position on the front and back surfaces represented by points p_f and p_b in primed coordinates (x', y), separated by the offset d'. The chopper blade is shown at two rotation angles: When the trailing edge of the front surface passes the beampath (blue), and when the trailing edge of the back surface passes, and unblocks, the beampath (red). The angle $\delta\theta$ between the two events is labeled. The leading and trailing edges of both surfaces are indicated as in (b).

edge of the front surface and the trailing edge of the back surface in (r, θ) coordinates. We model the finite chopper width using two offset ellipses, representing the front and back surfaces of the chopper. The offset d in (x, y) coordinates is given by the following equation.

$$d = w \sin(\eta) \tag{4.2}$$

The same offset in (x', y) coordinates:

$$d' = w \tan(\eta) \tag{4.3}$$

The calculation of $\delta\theta$ is performed by separately considering the position of the beam relative to the front and the back surfaces of the chopper. In the (x', y) plane, let the center of the front surface be the origin, and call the resulting coordinates of the beam position $p_f = (p_x, p_y)$. The distance between the center of the front

22

and back surfaces is d', therefore the beam position with respect to the back surface is $p_b = (p_x + d', p_y)$. Transforming these two positions into (r, θ) coordinates, and calculating the angle $\delta\theta$ between them, yields:

$$\delta\theta = \operatorname{atan2}(y, x' + d') - \operatorname{atan2}(y, x') \tag{4.4}$$

The beam intensity in (x, y) coordinates is taken to be gaussian:

$$I_0(x, y) = \exp\left[-(\frac{x - x_0}{2\sigma_x})^2 - (\frac{y - y_0}{2\sigma_y})^2\right] \tag{4.5}$$

Where (x_0, y_0) is the beam center and σ_x, σ_y are the beam widths along the x and y directions, obtained with knife-edge measurements and given as standard deviations. The effect of the chopper on the beam is modeled by a square wave function $S(t, p)$ that is defined, as a function of time t, for each point p in the chopper plane. At a given time t_0, if the point p is blocked (unblocked) by the chopper, the square wave $S(t_0, p)$ takes the value zero (one). Since we consider clockwise chopper rotation, the phase of the square wave at each point must be equal to $-\theta$. The period of the modulation is $T = \frac{2\pi}{n_c}$, with $n_c = \pi/\rho$ representing the total number of cutouts in the chopper. Lastly, the duty cycle of the square wave is obtained by substituting the result of (4.4) into (4.1). Let the square wave $S(t, p) = S(t, \mathrm{DC}, \theta)$ be defined with duty cycle DC, period T, and phase offset $-\theta$ as:

$$S(t, \mathrm{DC}, \theta) = \begin{cases} 1 & \frac{\mathrm{DC}}{100} T \geq (t - \theta) \bmod T \\ 0 & \text{otherwise} \end{cases} \tag{4.6}$$

The resulting beam intensity $I(t, \eta)$ can be calculated by taking the integral, over the chopper plane, of the original beam intensity I_0 multiplied by the square wave function S. This integral is most easily expressed in (r, θ) coordinates, and so an integration factor Λ is included to account for the transformation of $I_0(x, y)$ into curvilinear (r, θ) coordinates. The resulting beam intensity is calculated numerically from the following expression:

$$I(t, \eta) = \int_{r_{min}}^{r_{max}} dr \int_{0}^{2\pi} d\theta \ \ I_0(r, \theta, \eta) \cdot S(t, \mathrm{DC}, \theta) \cdot \Lambda(r, \theta, \eta) \tag{4.7}$$

Where $\Lambda(r, \theta, \eta) = r\cos(\eta)$ is the determinant of the Jacobian for the coordinate transform from (x, y)

to (r, θ) coordinates, and r_{min}, r_{max} are the minimum and maximum radii of the chopper cutouts. Finally, the frequency spectrum of the intensity is calculated using a Fourier transform:

$$I(\omega, \eta) = \int_{-\infty}^{\infty} I(t, \eta) e^{-2i\pi\omega t} dt \tag{4.8}$$

In the calculation above, culminating in equation (4.7), we have assumed the beam crosses the top half of the chopper blade. To very good approximation, the formulas derived will apply even if this assumption is false. However, with the main explanation complete, it is now worth noting a subtlety which has been neglected thus far. Namely, $\delta\theta$ appears to change sign for points below the x' axis. This reflects the fact that, for the bottom half of the chopper, the front and back surfaces have their respective roles reversed. Consider figure 2(b), but with the beam position moved to the fourth quadrant. It is now the leading edge of the *back* surface (red, dotted) that intersects, and blocks, the beam path first; and the trailing edge of the *front* surface that intersects the beam path last, and unblocks it. The effect in the mathematical description is a phase shift. For the top half, the beam is blocked at the same time as the front surface would block it, and is unblocked later. Conversely, for the bottom half, the beam is *un*blocked at the same time as the front surface would unblock it, but is blocked earlier. In both cases, the amount of extra time δt that the beam is blocked is given by:

$$\delta t = \frac{T(50 - DC)}{100} \tag{4.9}$$

Therefore the discrepancy can be accounted for with an (effective) phase shift in the square wave for points below the x' axis. The change is as follows:

$$t \rightarrow t + \delta t \ \text{ for } \ \theta \in [\pi, 2\pi], \tag{4.10}$$

It is convenient to define a shifted time t':

$$t'(t, \theta, \eta, r) = \begin{cases} t & 0 < \theta < \pi \\ t + \delta t & \text{otherwise} \end{cases} \tag{4.11}$$

Replacing time t with the shifted time t' on the right hand side of equation (4.7) yields the final and exact

expression for the beam intensity, given *any* beam position. The same Fourier transform described in equation (4.8) can be applied to the new intensity to calculate the exact frequency spectrum. The numerical results presented below were obtained using this method.

4.3 Spectrum Measurement

A SciTec Instruments (Model 300CD) mechanical chopper with a 10 slot blade was placed on a precision rotation mount to allow the angle η to be tuned. A MIRCAT Mid-IR Laser was used in Continuous Wave mode, at a 10.6μm wavelength. The laser was focused onto a 30μm linewidth platinum cross device with an identical beam path and optics as those described in section 4.2 of the main paper, "Photovoltage Measurement". The longitudinal voltage across the device was measured with an Ametek (Model 7230A) lock-in amplifier. After preliminary scans, the location with maximal longitudinal photocurrent response was identified. At that location, the response magnitude $I_{n\omega}(\eta)$ was then measured as a function of the angle η and the harmonic n above the chopper frequency ω (approximately 290 Hz).

4.4 Simulation

With angle $\eta = 0$, the beam was measured to intersect the chopper blade at $(x, y) = (6.35\text{mm}, 30.95\text{mm})$. Furthermore, using a standard knife-edge measurement, the beamwidths in the x and y directions were given by $\sigma_x = 2$mm and $\sigma_y = 1.6$mm. The chopper width was measured with a caliper to be 0.66mm, and the minimum and maximum radii of the chopper slots to be 19.05mm and 50.8mm, respectively.

With these initial values as input, a MATLAB script was used to perform a numerical approximation of the integral in equation (4.7) on an 8000×250 grid in (r, θ) space for one period T divided into 3000 individual timesteps. A fast Fourier transform was then performed on the time series data, and the relative magnitudes of the integer harmonics $n\omega$ were recorded. This process was performed for 20 equally-spaced angles of $\eta \in [0°, 80°]$ to obtain simulated magnitudes $I_{n\omega}(\eta)$ which are plotted alongside experimental data in Figure 4.3.

4.5 Results

The results of the simulation are promising. The reduction of the 1ω and 3ω responses with increasing angle η, unaccounted for by 2D chopper and line-like beam assumptions, are captured both quantitatively and qualitatively. The results also qualitatively explain the magnitude of the 3ω transverse response presented in Figure 3.4(b), in particular the deviation of $I_{3\omega}/I_{1\omega}$ from the naive value $I_{3\omega}/I_{1\omega} = 0.5$ obtained using the Fourier transform of a pure square wave. Furthermore, the simulation succeeds in qualitatively matching the finite experimental 2ω response, apart from some offset in magnitude. We suspect this offset arises as a consequence of the spatial variation of the longitudinal response, in combination with slight deviations in the widths of the chopper cutouts. Analysis of these factors is beyond the scope of this chapter.
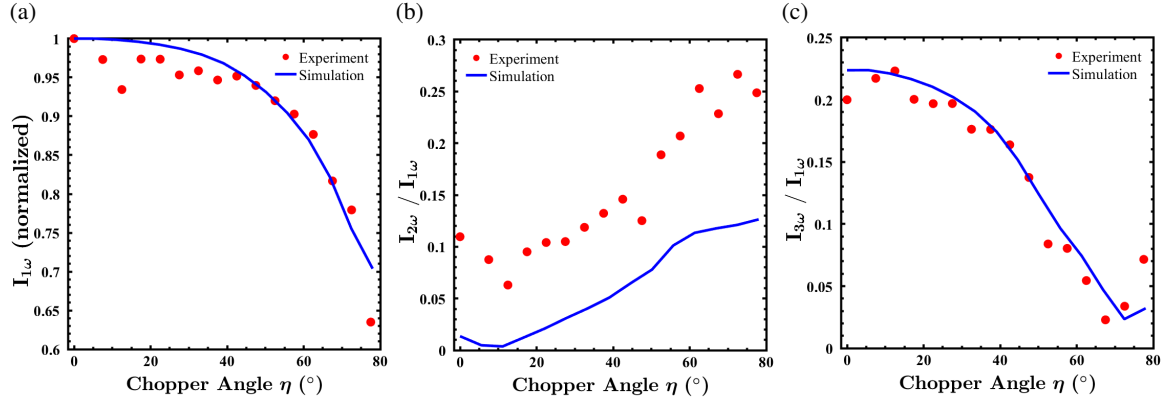

Figure 4.3: (a) Experimental and simulated results for the first harmonic of the longitudinal photocurrent response I at chopper frequency ω plotted as a function of angle η, normalized to be unity at $\eta = 0$. (b) Second harmonic of longitudinal photocurrent response as a function of angle η, presented as the ratio $I_{2\omega}/I_{1\omega}$ at each value of η. (c) Third harmonic of longitudinal photocurrent response as a function of angle η, presented similarly as the ratio $I_{3\omega}/I_{1\omega}$ at each value of η.

26

Bibliography

[1] Gavin B Osterhoudt, Laura K Diebel, Mason J Gray, Xu Yang, John Stanco, Xiangwei Huang, Bing Shen, Ni Ni, Philip JW Moll, Ying Ran, et al. Colossal mid-infrared bulk photovoltaic effect in a type-i weyl semimetal. *Nature materials*, 18(5):471–475, 2019.

[2] Qiong Ma, Adolfo G Grushin, and Kenneth S Burch. Topology and geometry under the nonlinear electromagnetic spotlight. *Nature materials*, 20(12):1601–1614, 2021.

[3] Andrei Bernevig, Hongming Weng, Zhong Fang, and Xi Dai. Recent progress in the study of topological semimetals. *Journal of the Physical Society of Japan*, 87(4):041001, 2018.

[4] Binghai Yan and Claudia Felser. Topological materials: Weyl semimetals. *Annual Review of Condensed Matter Physics*, 8(1):337–354, 2017.

[5] Zhi-Yu Chen, Lian-Shan Yan, Yan Pan, Lin Jiang, An-Lin Yi, Wei Pan, and Bin Luo. Use of polarization freedom beyond polarization-division multiplexing to support high-speed and spectral-efficient data transmission. *Light Sci. Appl.*, 6(2):e16207–e16207, August 2016.

[6] Yu-Xuan Wang, Xin-Yue Zhang, Chunhua Li, Xiaohan Yao, Ruihuan Duan, Thomas KM Graham, Zheng Liu, Fazel Tafti, David Broido, Ying Ran, et al. Visualization of bulk and edge photocurrent flow in anisotropic weyl semimetals. *Nature Physics*, 19(4):507–514, 2023.

[7] Daniel E Parker, Takahiro Morimoto, Joseph Orenstein, and Joel E Moore. Diagrammatic approach to nonlinear optical response with application to weyl semimetals. *Phys. Rev. B.*, 99(4), January 2019.

[8] Philippe Gagnon, Monique Tie, Pierre L Levesque, Benoit C St-Antoine, Patrick Desjardins, and Richard Martel. Direct measurement of the absolute seebeck coefficient using graphene as a zero coefficient reference. *J. Phys. Chem. C Nanomater. Interfaces*, 128(30):12657–12662, August 2024.

[9] Masataka Hase, Daiki Tanisawa, Kaito Kohashi, Raichi Kamemura, Shugo Miyake, and Masayuki Takashiri. Determination of seebeck coefficient originating from phonon-drag effect using si single crystals at different carrier densities. *Sci. Rep.*, 13(1):13463, August 2023.

[10] MM Glazov and SD Ganichev. High frequency electric field induced nonlinear effects in graphene. *Physics Reports*, 535(3):101–138, 2014.

[11] Xiaodong Xu, Nathaniel M Gabor, Jonathan S Alden, Arend M Van Der Zande, and Paul L McEuen. Photo-thermoelectric effect at a graphene interface junction. *Nano letters*, 10(2):562–566, 2010.

[12] P L Richards. Bolometers for infrared and millimeter waves. *J. Appl. Phys.*, 76(1):1–24, July 1994.

[13] Mikhail N Polyanskiy. Refractiveindex. info database of optical constants. *Scientific Data*, 11(1):94, 2024.

[14] Rei Kitamura, Laurent Pilon, and Miroslaw Jonasz. Optical constants of silica glass from extreme ultraviolet to far infrared at near room temperature. *Applied optics*, 46(33):8118–8133, 2007.

[15] COMSOL Multiphysics. COMSOL Multiphysics Software: Understand, Predict, and Optimize Physics-Based Designs and Processes, 2024. Accessed: 2024-11-13.

[16] Vincent Plisson, Piyush Sakrikar, Cameron Grant, Dylan Rosenmerkel, Gabriel Natale, Michael Geiwitz, Ying Ran, Krzysztof Kempa, and Kenneth S. Burch. Transverse photoresistivity from photothermal current deflection in metal films. *ArXiv*, 2025.

[17] Mason J Gray, Narendra Kumar, Ryan O'Connor, Marcel Hoek, Erin Sheridan, Meaghan C Doyle, Marisa L Romanelli, Gavin B Osterhoudt, Yiping Wang, Vincent Plisson, et al. A cleanroom in a glovebox. *Review of Scientific Instruments*, 91(7), 2020.